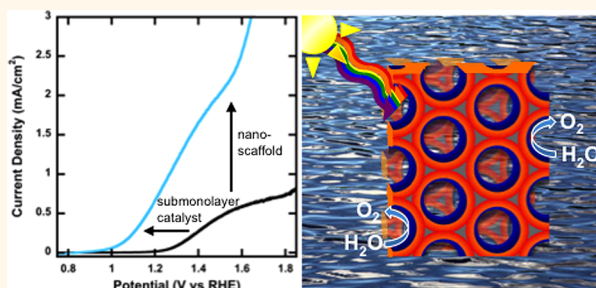


# Atomic Layer Deposition of a Submonolayer Catalyst for the Enhanced Photoelectrochemical Performance of Water Oxidation with Hematite

Shannon C. Riha,<sup>†,‡,▲</sup> Benjamin M. Klahr,<sup>§,▲</sup> Eric C. Tyo,<sup>||</sup> Sönke Seifert,<sup>⊥</sup> Stefan Vajda,<sup>†,||,¶</sup> Michael J. Pellin,<sup>†,‡</sup> Thomas W. Hamann,<sup>§,\*</sup> and Alex B. F. Martinson<sup>†,‡,\*</sup>

<sup>†</sup>Materials Science Division, Argonne National Laboratory, Argonne, Illinois 60439, United States, <sup>‡</sup>Argonne—Northwestern Solar Energy Research (ANSER) Center, Argonne National Laboratory, Argonne, Illinois 60439, United States, <sup>§</sup>Department of Chemistry, Michigan State University, East Lansing, Michigan 48824-1322, United States, <sup>⊥</sup>X-ray Science Division, Argonne National Laboratory, Argonne, Illinois 60439, United States, <sup>||</sup>Department of Chemical and Environmental Engineering, School of Engineering & Applied Science, Yale University, New Haven, Connecticut 06520, United States, and <sup>¶</sup>Nanoscience and Technology Division, Argonne National Laboratory, Argonne, Illinois 60439, United States. <sup>▲</sup>These authors contributed equally.

**ABSTRACT** Hematite photoanodes were coated with an ultrathin cobalt oxide layer by atomic layer deposition (ALD). The optimal coating—1 ALD cycle, which amounts to <1 monolayer of  $\text{Co(OH)}_2/\text{Co}_3\text{O}_4$ —resulted in significantly enhanced photoelectrochemical water oxidation performance. A stable, 100–200 mV cathodic shift in the photocurrent onset potential was observed that is correlated to an order of magnitude reduction in the resistance to charge transfer at the  $\text{Fe}_2\text{O}_3/\text{H}_2\text{O}$  interface. Furthermore, the optical transparency of the ultrathin  $\text{Co(OH)}_2/\text{Co}_3\text{O}_4$  coating establishes it as a particularly advantageous treatment for nanostructured water oxidation photoanodes. The photocurrent of catalyst-coated nanostructured inverse opal scaffold hematite photoanodes reached 0.81 and 2.1  $\text{mA}/\text{cm}^2$  at 1.23 and 1.53 V, respectively.



**KEYWORDS:** hematite ·  $\text{Fe}_2\text{O}_3$  · photoelectrocatalysis · water oxidation · electrochemical impedance spectroscopy · X-ray absorption spectroscopy · XANES

Solar radiation is a renewable energy source that has the capacity to meet global energy demands in a carbon-neutral fashion. As such, many devices have been developed and optimized to capture and convert solar energy into electricity.<sup>1,2</sup> However, because solar energy is diffuse and intermittent, an efficient and economically viable method to concentrate and store energy harvested from the sun must be realized. One method is to store solar energy in the form of chemical bonds—much like in photosynthesis—through photoelectrochemical (PEC) water splitting.<sup>3–6</sup> Since Fujishima and Honda's seminal report,<sup>7</sup> extensive research has been devoted toward identifying a material capable of meeting the

strict requirements necessary for large-scale implementation.<sup>1,4,8–13</sup>

Hematite ( $\alpha\text{-Fe}_2\text{O}_3$ ) is one promising material that meets many of the requirements for the water oxidation half reaction: (i) it has a suitable band gap of 2.0–2.1 eV; (ii) it is stable under water oxidation conditions, often in alkaline electrolytes; and (iii) it is composed of earth-abundant and nontoxic elements, making it environmentally benign and inexpensive.<sup>8–10,14</sup> Despite such promising attributes, the overall water splitting efficiency of hematite photoanodes falls well short of the theoretical maximum efficiency.<sup>4,15</sup> A short hole collection distance, coupled with comparatively long light penetration depths, is one factor limiting the efficiency of hematite photoanodes.

\* Address correspondence to  
martinson@anl.gov,  
hamann@chemistry.msu.edu.

Received for review December 6, 2012  
and accepted February 12, 2013.

Published online February 12, 2013  
10.1021/nn305639z

© 2013 American Chemical Society

Nanostructured photoelectrode architectures have begun to address current materials limitations by decoupling light absorption and charge carrier extraction. There have been several reports detailing the nanostructuring of hematite with improved PEC performance that fall into two categories: (i) morphology control, including nanoparticles,<sup>16</sup> nanowires,<sup>17–19</sup> nanorods,<sup>20</sup> and nanocaliflower;<sup>21</sup> and (ii) scaffolding, whereby a film with thickness on the order of the hole collection distance is folded over a high surface area architecture.<sup>9,22–25</sup> The general consensus is that, for hematite to be useful for solar energy conversion and storage, nanostructuring is imperative.

Another characteristic limiting efficiency is sluggish oxygen evolution reaction (OER) kinetics at the surface of hematite photoanodes, thus requiring a large applied potential to drive water oxidation. Tilley *et al.* demonstrated that  $\text{IrO}_2$  nanoparticles coupled to the surface of hematite reduced the photocurrent onset potential by 0.2 V, although the catalyst is not stable over time.<sup>26</sup> Adding nickel oxide or cobalt-based catalysts (cobalt ions,  $\text{Co}^{2+}$ , the cobalt phosphate catalyst, "Co-Pi", or  $\text{Co}_3\text{O}_4$ ) is equally interesting as they offer low-cost alternatives to the rare and expensive Ir- and Ru-based catalysts yet provide a similar reduction in the overpotential and improvement in photocurrent.<sup>21,27–36</sup> For instance, the addition of Co-Pi to the surface of hematite has recently received much attention. Electrodeposited films show on average a respectable 200 mV cathodic shift in the photocurrent onset potential, as well as stability due to a "self-healing" mechanism in the presence of phosphate buffer.<sup>28,29,31–34</sup>

The requirement for nanostructuring hematite presents a potential challenge for coupling many well-known water oxidation catalysts to the surface. For example, the few hundred nanometers of porous Co-Pi necessary to see the full onset shift would be difficult to achieve on all surfaces of state-of-the-art nanocaliflower hematite since the pore size is on the order of several nanometers.<sup>29,37</sup> Second, the competitive light absorption of many catalysts poses an even greater obstacle within nanostructured architectures.<sup>30,32</sup> Xi *et al.* showed that even nanoparticles of  $\text{Co}_3\text{O}_4$  on the surface of hematite nanorods significantly alter the absorption of the photoanode.<sup>30</sup> Finally, the catalyst coating must be deposited uniformly on the surface of hematite at the top, as well as deep within the nanostructured architecture, without variation in coating thickness or clogging of the porous structure. For example, Co-Pi films are typically deposited by electrodeposition, which requires consistent conductivity across the entire semiconductor photoanode to produce a uniform film. If the semiconductor is nanostructured and the FTO substrate is exposed, the Co-Pi will preferentially grow on the FTO substrate because of its higher conductivity.<sup>31</sup> This can be alleviated using

photoelectrodeposition, such that the film can deposit onto all areas that have photogenerated holes,<sup>29,33,38</sup> however, the process is not self-limiting and can result in clogged pores of a nanostructured architecture. Dip-coating or wet impregnation methods have also been utilized as an alternative to electrodeposition to deposit one monolayer of  $\text{Co}^{2+}$  catalyst,<sup>21,28,33,39,40</sup> but this approach suffers in terms of catalyst longevity on the surface.<sup>28</sup>

Herein, we demonstrate the potential of using atomic layer deposition (ALD) to deposit a Co-based catalyst on the surface of hematite photoanodes with both flat and nanostructured geometries. ALD is uniquely suited to the deposition of conformal catalytic overlayers on nanostructures, due to its self-limiting, vapor-phase surface chemistry and angstrom-level thickness control.<sup>41–45</sup> The self-limiting surface chemistry further enables an identical catalyst overlayer to be deposited on various architectures—flat or nanostructured—with excellent reproducibility. In addition, ALD is a desirable fabrication method due to low deposition temperatures (<250 °C) and mild vacuum conditions, coupled with the inexpensive precursors used for the processes discussed below. We observe that the catalyst overlayer does not compete with hematite for light absorption and demonstrates remarkable stability under PEC water oxidation conditions. Furthermore, the role of the ALD catalyst overlayer was analyzed by photoelectrochemical impedance spectroscopy, given that the role of Co-based overlayers on hematite has been a subject of much debate.<sup>46</sup> Our results demonstrate that less than one monolayer (ML) of the Co-based catalyst deposited by ALD exhibits a significant reduction in the resistance to charge transfer (catalysis), resulting in performance comparable to a similar hematite photoanode with 1000× thicker Co-Pi coating.

## RESULTS AND DISCUSSION

**Evaluation of Catalyst Overlays.** Photoanodes were prepared by coating flat fluorine-doped tin oxide (FTO)-coated glass substrates and inverse opal scaffolds on FTO-coated glass (herein simply referred to as inverse opal scaffolds) with tin-doped indium oxide (ITO) *via* ALD in order to produce a uniform and consistent conductive surface. The two types of substrates were subsequently coated with hematite *via* ALD. The thickness of the ITO and hematite layers in the nanolaminate was verified by ellipsometry on witness Si substrates and were 9 and 13 nm, respectively. Following postdeposition annealing at 500 °C in  $\text{O}_2$ , the hematite nanolaminate photoanodes were subjected to the ALD of either 1, 3, or 12 cycles of  $\text{CoCp}_2/\text{O}_3$ . Control electrodes were exposed to identical conditions except without the  $\text{CoCp}_2$  pulse. Based on a growth rate per cycle of the Co layer of 0.06 nm (determined by ellipsometric measurements of nanometer thick films),

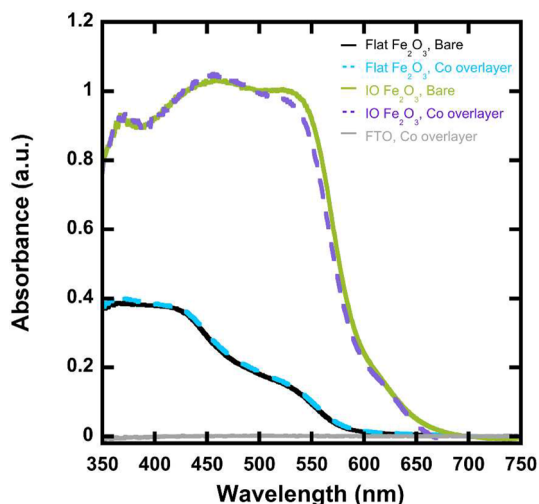


**Figure 1.** Reflectance-corrected absorbance spectra of a 13 nm flat hematite nanolaminate photoanode (black), 13 nm flat hematite nanolaminated photoanode coated with 1 ALD cycle  $\text{CoCp}_2/\text{O}_3$  (blue, dashed), 13 nm hematite nanolaminate on an inverse opal scaffold (green), 13 nm hematite nanolaminate on an inverse opal scaffold coated with 1 ALD cycle (purple, dashed), and 1 ALD cycle on bare FTO-coated glass (gray).

1 cycle corresponds to  $<1$  ML of catalyst (Supporting Information Figure S1).

Figure 1 shows the absorbance of bare hematite photoanodes compared to those with 1  $\text{CoCp}_2/\text{O}_3$  ALD cycle for both flat substrates and inverse opal scaffolds. Even for nanostructured electrodes, it is clear that the ultrathin overlayers do not alter the total absorption of the photoanode. The fact that there is no competitive absorption even on the high-area inverse opal scaffolds makes this an ideal catalyst for nanostructured and porous photoanodes. Moreover, this transparency is in stark contrast to the absorptivity of other known overlayers (including  $\text{Co-Pi}$ ,<sup>28</sup>  $\text{Co}_3\text{O}_4$ ,<sup>30</sup>  $\text{IrO}_x$ <sup>47</sup>) on hematite.

Photoelectrochemical current density *versus* applied potential ( $J-E$ ) measurements were performed on bare hematite photoanodes, as well as those coated with the Co-based overlayer, in 0.1 M KOH aqueous electrolyte (pH 13.1). The light  $J-E$  curves are plotted in Figure 2 (with dark currents in Figure S2a). Flat, bare hematite photoanodes exhibit the typical response of ALD-grown planar hematite electrodes in pH 13 electrolyte,<sup>23,29,48</sup> with a photocurrent onset potential of +1.25 V vs RHE. The photocurrent rises until it reaches a plateau current of 0.65  $\text{mA}/\text{cm}^2$  around 1.5 V vs RHE before the dark current starts to onset at 1.8 V. The bare hematite inverse opal scaffold shows a slightly earlier onset potential of 1.1 V vs RHE, which is expected for a larger interfacial area for oxygen evolution per projected (geometric) area. Due to greater light-harvesting efficiency relative to the flat photoanode, the photocurrent further increases rapidly and reaches 1.5  $\text{mA}/\text{cm}^2$  at 1.53 V vs RHE.

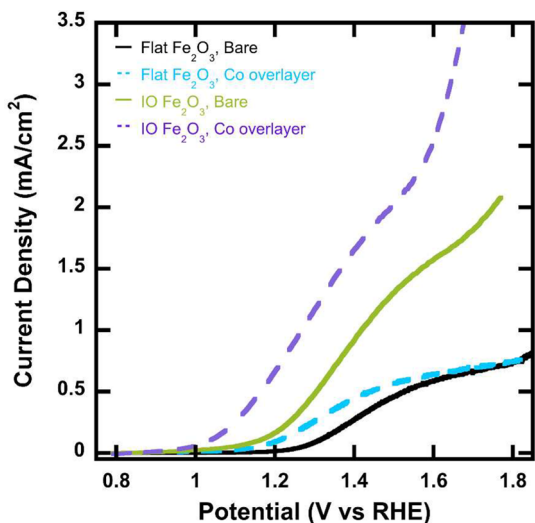


**Figure 2.**  $J-E$  curves for 13 nm hematite photoanodes on a flat FTO-ITO substrate (black), on an ITO-coated inverse opal scaffold (green), on an equivalent flat electrode further coated with 1  $\text{CoCp}_2/\text{O}_3$  ALD cycle (blue, dashed), and on an equivalent inverse opal scaffold further coated with 1  $\text{CoCp}_2/\text{O}_3$  ALD cycle (purple, dashed). Performance was measured at pH 13.1 under  $\sim 1$  sun illumination.

After just one ALD cycle of  $\text{CoCp}_2/\text{O}_3$ , the onset of photocurrent of the planar photoanode significantly shifts cathodically by  $\sim 100$  mV. The less desirable  $J-E$  response upon additional ALD coating can be found in Figure S2b. The current onset potential is even more pronounced for the inverse opal scaffold geometry, showing a 200 mV cathodic shift to onset at  $\sim 0.95$  V vs RHE. In addition, the photocurrent plateau increased substantially for the Co-modified nanostructured photoelectrode, from 1.4 to 2.1  $\text{mA}/\text{cm}^2$  at 1.53 V vs RHE. This value is comparable to some of the best devices reported using Co-based catalysts.<sup>27,32,34</sup> This is a striking result in light of the submonolayer thickness of the deposition that results from just 1 ALD cycle. For comparison, a Co-Pi film of at least 8 nm is required to see a similar  $J-E$  enhancement, which can result in competitive light absorption and mass transport issues.<sup>29</sup>

In order for the catalyst to be useful, it must also be stable in the long term. The catalytic effect of  $\text{Co}^{2+}$  ions deposited from solution has been shown to degrade during prolonged measurements, requiring the  $\text{Co}^{2+}$  wet impregnation treatment to be repeated.<sup>28</sup> While the performance enhancement is recovered, having to reapply catalyst is not an ideal solution to the long-term utilization of such devices. On the other hand, Co-Pi exhibits long-term stability in the presence of phosphate, as phosphate assists in a “self-healing” mechanism of the Co-Pi catalyst.<sup>49</sup> The stability of 1  $\text{CoCp}_2/\text{O}_3$  ALD cycle on hematite nanolaminate photoanodes, as well as the stability of a bare hematite nanolaminate photoanode, is shown in Figure 3. The stability was monitored at two potentials, 1.23 and 1.53 V vs RHE, in 0.1 M KOH electrolyte under

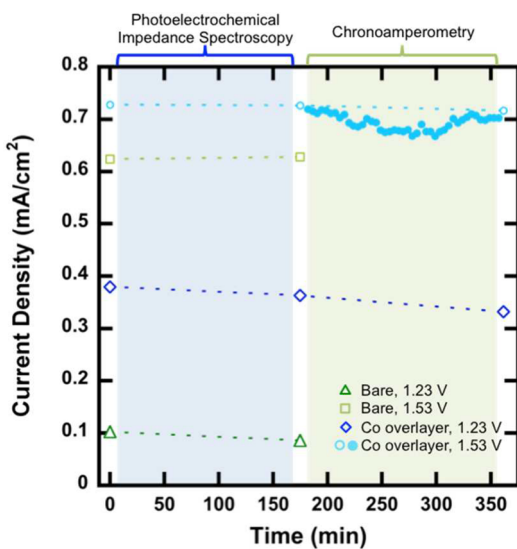


**Figure 3.** Stability of the photocurrent density as a function of time in 0.1 M KOH under 1 sun illumination. The photocurrent density was monitored at 1.23 and 1.53 V vs RHE for bare (dark green triangles = 1.23 V, light green squares = 1.53 V) and 1 CoCp<sub>2</sub>/O<sub>3</sub> ALD cycle on (dark blue diamonds = 1.23 V, and light blue circles = 1.53 V) hematite nanolaminate photoanodes. The open symbols denote data collected from  $J-E$  scans (Supporting Information Figure S3) taken at various times during photoelectrochemical characterization, while closed symbols represent data collected at a constant potential of 1.53 V vs RHE.

~1 sun illumination. At 1.23 V vs RHE, the photocurrent of the bare hematite photoanode decreased by 16% during the first 3 h period, while the sample coated with 1 ALD cycle decreased by 12% after a total of 6.5 h. These changes are largely within the combined error of the measurement that includes lamp intensity drift. Regardless, the overlayer is clearly not an additional source of performance loss over hours. At an applied potential of 1.53 V vs RHE, the bare hematite sample current density remains largely unchanged, while the overlayer-modified photoanode exhibits only a 1.5% decrease after 6.5 h. Again, the fluctuations observed are most easily attributed to light intensity variations of the Xe lamp over the long constant potential measurement. The stability of the Co-based overlayer is further demonstrated in Figure S3, where the current onset potential remains significantly more cathodic than the bare photoelectrode control and the plateau currents remain unchanged after impedance testing.

**Phase Identification of Co-Based Overlayer.** The ALD-grown cobalt-based overlayer shows several advantages over other OER catalysts in the literature, including virtually no competitive optical absorption, stability over hours, and its ability to significantly enhance the PEC performance of hematite photoanodes. Therefore, understanding the nature of the submonolayer catalyst is a worthy, if challenging, goal. Determining the chemical makeup of the Co-based catalyst is a challenging task due to the very limited amount of Co present on the surface. As such, structural characterization

techniques such as grazing-incidence X-ray diffraction are not possible. More surface-sensitive techniques such as X-ray photoelectron spectroscopy (XPS) and X-ray absorption near-edge spectroscopy (XANES) were therefore applied to identify the composition and Co oxidation state of the catalyst layer.

XPS was used to analyze freshly prepared Co-ALD layers to determine if the initial composition contains a mixture of Co(II) and Co(III) oxides and hydroxides. Figures 4a and S4 reveal detailed spectra over the Co 2p region showing the spin-orbit splitting into Co 2p<sub>3/2</sub> and Co 2p<sub>1/2</sub> components for a Co<sub>3</sub>O<sub>4</sub> standard, 1 ALD cycle, 3 ALD cycles, and 12 ALD cycles of Co-based catalyst. CoO and Co(OH)<sub>2</sub> standards were also investigated; however, it was found that the surface of these standards was significantly oxidized. While the main Co 2p<sub>3/2</sub> peak for the ALD-grown Co catalyst is at 780.7 and 779.5 eV for the Co<sub>3</sub>O<sub>4</sub> standard, the binding energies of the most intense peaks alone cannot be used to distinguish between the different oxides, as the binding energy of various oxide and hydroxide forms overlap.<sup>50–56</sup> However, there is a more apparent difference in the XPS spectra for pure Co(II) and Co(III). In 3d transition metals that have unpaired electrons (such as Co(II)), additional spectral lines, known as satellite line structure, result. In Figure 4a, a broad satellite peak centered at 786.3 eV was observed for all of the Co-based overlayers deposited by ALD. In contrast, this feature is clearly missing in the Co<sub>3</sub>O<sub>4</sub> high-resolution spectrum. This suggests that a freshly deposited ultrathin Co-based ALD coating does not contain a significant fraction of Co<sub>3</sub>O<sub>4</sub>, rather it consists mostly of Co(II). To further quantify the composition of the Co-ALD layer, the most intense Co 2p<sub>3/2</sub> peak and the associated satellite lines were fit using parameters from literature.<sup>56</sup> The fitting results suggest that a freshly deposited Co-ALD layer consists of 90% Co(II), in the form of either Co(OH)<sub>2</sub> or CoO, and ~10% Co<sub>3</sub>O<sub>4</sub>. This result is in contrast to that determined for thick cobalt oxide films deposited by the same ALD process, as well as literature precedence,<sup>57</sup> which exhibit the characteristic reflections of Co<sub>3</sub>O<sub>4</sub> and not Co(II) species.

XANES has been successfully utilized to determine chemical composition and monitor changes occurring during reaction processes for subnanometer to nanometer particles previously.<sup>58–61</sup> XANES spectrum collected from a 12 ALD cycle cobalt sample (post-PEC analysis) is presented in Figure 4b, together with the spectra of the relevant cobalt standards. Additional cobalt oxide and hydroxide standards are found in Figure S5. Because of the overlap with the Fe and Co edge, XANES data were collected only from a hematite nanolaminate photoanode with 12 ALD cycles of CoCp<sub>2</sub>/O<sub>3</sub> to ensure that the Co signal was above the noise. A linear combination fitting was used to determine the composition of the sample. All combinations

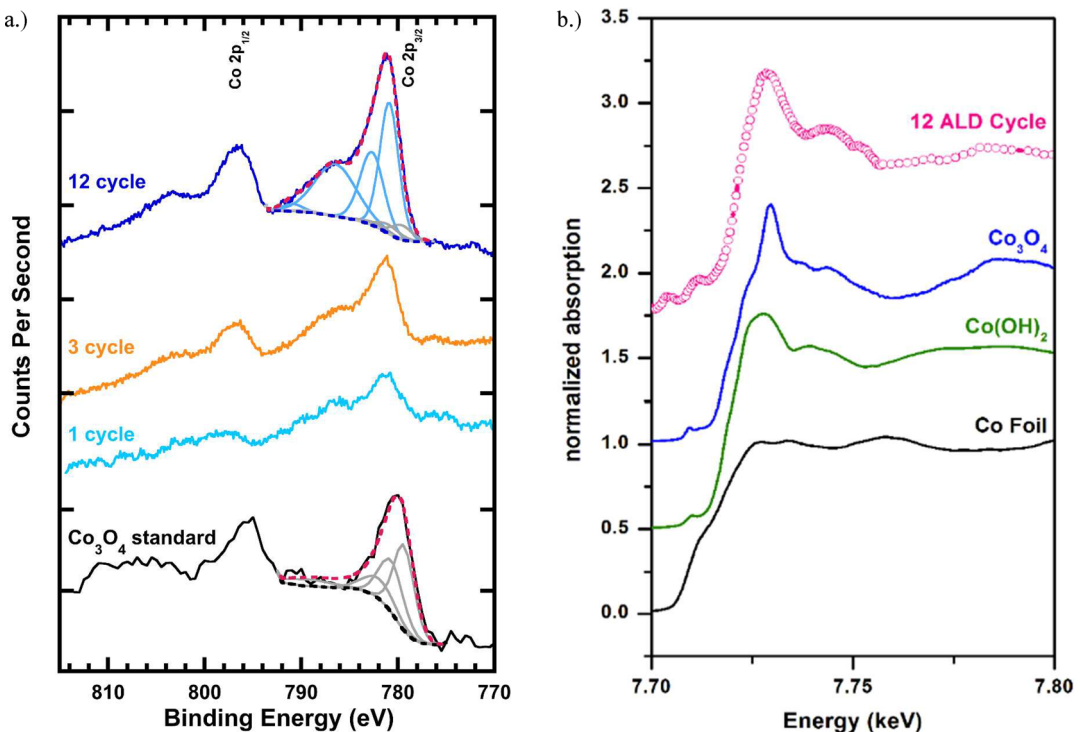


**Figure 4.** (a) XPS spectra of Co<sub>3</sub>O<sub>4</sub> standard (black), freshly prepared hematite nanolaminate coated with 1 (blue), 3 (orange), and 12 (dark blue) ALD cycles of Co-based catalyst. The data in the XPS spectra for the Co<sub>3</sub>O<sub>4</sub> standard and the 12 ALD cycle sample were fit using the fitting constants presented in Table S1. (b) XANES spectra of Co foil (black), Co(OH)<sub>2</sub> standard (green), Co<sub>3</sub>O<sub>4</sub> standard (blue), and hematite nanolaminate coated with 12 ALD cycles of Co-based (magenta) catalyst post-PEC analysis.

of possible compositions were attempted using the following bulk standards: Co<sub>3</sub>O<sub>4</sub>, Co<sub>2</sub>O<sub>3</sub>, CoO, Co(OH)<sub>2</sub>, Fe<sub>2</sub>CoO<sub>4</sub>, and metallic cobalt. The best fit results were obtained for a composition with a ratio of 2:1 for Co<sub>3</sub>O<sub>4</sub> to Co(OH)<sub>2</sub>, respectively, for the 12 ALD cycle sample following PEC analysis. These data, coupled with XPS data, suggest that the initial composition of the Co-ALD layer consisted mainly of Co(II). After electrochemical testing in alkaline media, the Co-ALD layer is identified as the same species but in different proportion.

**Role of Co(II)/Co<sub>3</sub>O<sub>4</sub> Catalyst on Hematite Nanolaminate Photoanodes.** The role that overlayers play on the surface of hematite has been of much debate in the recent literature<sup>28,29,32,33,35,46,62</sup> given that similar effects have been observed with noncatalytic overlayers used for surface passivation,<sup>27,63</sup> as well as the formation of p–n junctions at the surface.<sup>36,48,64</sup> There is limited evidence for a true catalytic effect of the overlayer,<sup>29</sup> passivation of surface states and increased band bending are more often deduced as effects of overlayers.<sup>27,28,39,40,63</sup> Therefore, electrochemical impedance spectroscopy was performed on the flat electrodes to further understand the improvement that the submonolayer Co(II)/Co<sub>3</sub>O<sub>4</sub> endows upon hematite photoanodes. Nyquist plots measured under illumination at an applied potential of 1.27 V vs RHE are shown in Figure 5 for both a bare and Co(II)/Co<sub>3</sub>O<sub>4</sub>-modified photoanodes. At this potential, both electrodes show two clear semicircles, but the resistance of the low-frequency

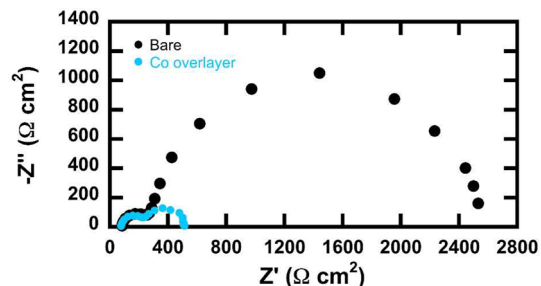


**Figure 5.** Nyquist plot measured at an applied potential of 1.27 V vs RHE under 1 sun illumination for a bare hematite nanolaminate photoanode (black circles) and a hematite nanolaminate coated with 1 ALD cycle Co(II)/Co<sub>3</sub>O<sub>4</sub> (blue squares).

semicircle is greatly reduced for the photoanode with the Co-overlayer. The equivalent circuit shown in Figure 6 is considered for fitting the IS data.<sup>29,65</sup> This equivalent circuit consists of the capacitance of the bulk hematite thin film, C<sub>bulk</sub>, a resistance to electrons recombining with holes in surface states, R<sub>rec</sub>, a capacitance of the surface states, C<sub>ss</sub>, and a charge transfer resistance from the surface states, R<sub>ct,ss</sub>. This equivalent circuit was selected by making the assumption that charge transfer occurs through surface states, an assumption which has been tested and discussed previously.<sup>66</sup> At the most positive potentials, a distinct low-frequency semicircle can no longer be resolved and the single semicircle may be fit with a Randles circuit (Figure S6) which omits C<sub>ss</sub> and R<sub>ct,ss</sub>. The disappearance of this low-frequency semicircle

has been previously attributed to the rapid charge transfer from oxidized surface states which prevents significant charge buildup and an immeasurably small  $C_{ss}$  and  $R_{ct,ss}$ .<sup>70</sup> Since both bare and Co(II)/ $\text{Co}_3\text{O}_4$ -modified hematite nanolaminate photoanodes show similar Nyquist plots and  $J-E$  curves, the same equivalent circuits were used for interpreting both electrodes.

Fitting the IS data yields the equivalent circuit parameters shown in Figures 7 and S7 for bare and Co(II)-modified hematite nanolaminate photoanodes. After addition of Co(II)/ $\text{Co}_3\text{O}_4$ , the  $C_{bulk}$  values remain largely unchanged as expected (Figure S7a).  $C_{bulk}$  values decrease with increasing positive applied potential, which is consistent with Mott–Schottky (MS) behavior of an n-type semiconductor. MS plots were prepared from  $C_{bulk}$  values measured under both dark and illuminated conditions (Figure 7a). Derived flat band potentials,  $E_{FB}$ , in the dark of 0.744 and 0.735 vs RHE were essentially identical for bare and coated hematite electrodes, respectively. The dopant density,  $N_D$ , was derived from the slope of the MS plots, producing values of  $1.1 \times 10^{19}$  and  $1.6 \times 10^{19} \text{ cm}^{-3}$  for bare and Co(II)/ $\text{Co}_3\text{O}_4$ -coated electrodes respectively. This suggests that the enhanced performance of the coated hematite electrodes is not due to a shift in the flat band potential. The MS data flatten at potentials greater than

approximately 1.4 V vs RHE. This is likely due to the thin film becoming fully depleted at these positive potentials, such that applying further positive potentials does not decrease the bulk capacitance. This can be confirmed by calculating the maximum depletion width ( $W_{max}$ ) with the equation

$$W_{max} = \sqrt{\frac{2k\epsilon_0 V_{max}}{qN_D}}$$

where  $k$  is the dielectric constant of the semiconductor (taken to be 32),  $\epsilon_0$  is the permittivity of a vacuum ( $8.854 \times 10^{-12} \text{ C V}^{-1} \text{ m}^{-1}$ ),  $q$  is the charge of an electron,  $N_D$  is the dopant density, and  $V_{max}$  is the voltage dropped across the entire hematite film.<sup>67–69</sup> The  $V_{max}$  was calculated as the voltage difference between the  $E_{FB}$  and the potential at which the MS plot plateaus ( $\sim 1.4$  V). The maximum depletion width or thicknesses of the electrodes were calculated to be 12 and 14 nm for the bare and Co(II)/ $\text{Co}_3\text{O}_4$ -coated electrodes, respectively. This is in excellent agreement with the thickness of these films as measured by ellipsometry and absorption spectroscopy (13 nm). This expected space-charge capacitance behavior of the measured  $C_{bulk}$  further validates our equivalent circuit and the use of MS analysis.

The  $C_{ss}$  for both photoanodes (Figure 7b) shows a peak which corresponds with the current inflection potential (Figure 2) and similarly shifts  $\sim 100$  mV with the Co(II)/ $\text{Co}_3\text{O}_4$  modification. The magnitude of the peak is also decreased for the coated photoanode compared to the bare hematite nanolaminate. This is consistent with charge transfer from the surface states of Co(II)/ $\text{Co}_3\text{O}_4$ -modified photoanodes being faster than charge transfer from the surface states of bare electrodes since fast hole transfer will yield a lower steady-state hole concentration in the surface states and thus a lower capacitance. This suggests that the role of the Co(II)/ $\text{Co}_3\text{O}_4$  layer is to accelerate charge transfer kinetics, that is, act as a true water oxidation catalyst. This same trend was also observed by measuring the charge passed through cathodic current transients<sup>29,70</sup> measured in response to turning off 1 sun illumination (Figure S8).

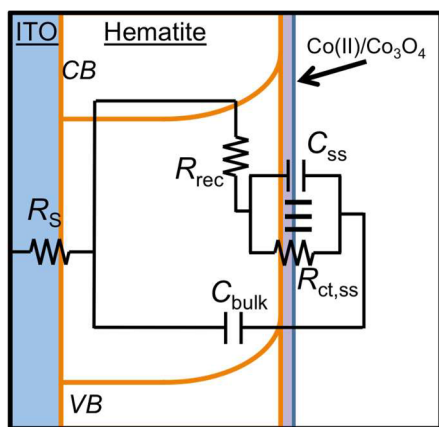


Figure 6. Equivalent circuit used for water oxidation at hematite electrodes.

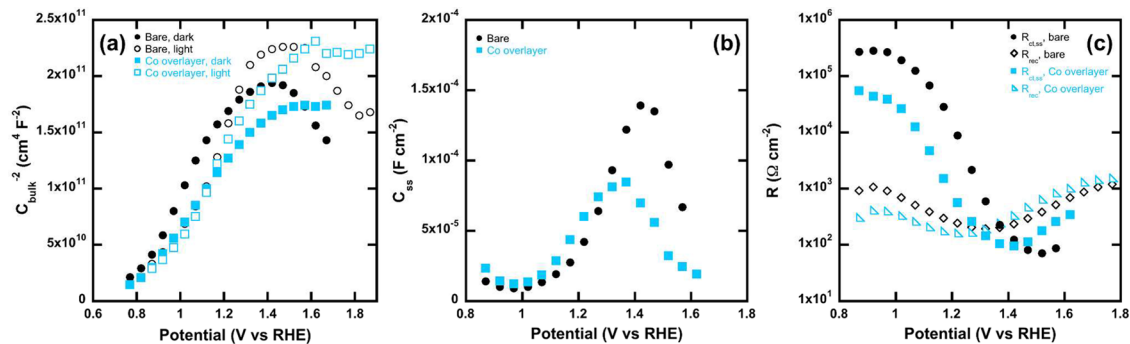


Figure 7. Representative (a)  $C_{bulk}$  measured in the dark (closed symbols) and under 1 sun illumination (open symbols), (b)  $C_{ss}$  and (c)  $R_{rec}$  (open symbols) and  $R_{ct,ss}$  (closed symbols) for a bare hematite photoanode (black symbols) and a nominally identical hematite with 1 ALD cycle Co(II)/ $\text{Co}_3\text{O}_4$  (blue symbols).  $C_{ss}$ ,  $R_{rec}$ , and  $R_{ct,ss}$  data were collected under 1 sun illumination.

It could be argued that the reduction in  $C_{ss}$  observed may be attributed to a passivation of some surface states, similar to the effect seen with group 13 overayers.<sup>27,63</sup> By examining  $C_{ss}$  at potentials less than the photocurrent onset, the effects of water oxidation kinetics can be eliminated. From 0.8 to 1.0 V, the  $C_{ss}$  (and integrated cathodic current transient) is equal to or slightly larger than that for the Co-modified photoelectrode, which suggests that surface states are not passivated by the overlayer. More direct evidence that the overlayer is acting to catalyze the OER reaction can be uncovered by comparing the resistance to charge transfer across the electrochemical interface (Figure 7c). For both photoanodes,  $R_{ct,ss}$  decreases with more positive applied potentials until  $R_{ct,ss}$  becomes consistently low. At these potentials, the photocurrent, now controlled primarily by the flux of holes reaching the hematite surface, plateaus. For both photoelectrodes, the photocurrent onset potential is the same potential at which  $R_{ct,ss}$  is first within 2 orders of magnitude of  $R_{rec}$ . Intuitively, this is the point at which the water oxidation pathway becomes competitive with recombination—the competing pathway for oxidizing equivalents on the surface. A rigorous treatment of the kinetic parameter for charge transfer ( $k_{ct}$  water oxidation) reveals it to be proportional to the ratio  $R_{rec}/R_{ct,ss}$ .<sup>65</sup> Therefore, the order of magnitude lower  $R_{ct,ss}$  measured for the Co(II)/ $\text{Co}_3\text{O}_4$ -modified photoanode, with all else being equal, directly results in faster water oxidation kinetics on the Co(II)/ $\text{Co}_3\text{O}_4$  surface compared to the surface of hematite. This strong correlation between  $R_{rec}/R_{ct,ss}$  and photocurrent onset (Figure S9) further supports the conclusion that an acceleration of the rate of water oxidation alone can account for the cathodic shift observed. A similar  $R_{ct,ss}$  versus potential was observed upon coating a comparable hematite photoanode with  $\sim 15$  nm of the porous Co-Pi catalyst.<sup>29</sup> It should be noted, however, that the decrease in  $R_{ct}$  of Co-Pi-coated hematite films is largely a result of the greater surface area available for charge transfer to the electrolyte, due to the porous nature of the Co-Pi. The surface roughness of the  $<0.1$  nm thick Co(II)/ $\text{Co}_3\text{O}_4$  layer is not expected to alter the surface area of the photoanode, thus we can attribute the lower  $R_{ct,ss}$  to faster specific charge transfer kinetics (per area). The decrease in  $R_{ct,ss}$  with the addition of Co(II)/ $\text{Co}_3\text{O}_4$  is also evidence against a surface-state passivation mechanism since  $R_{ct,ss}$  would be expected to increase with the passivation of reactive surface states.<sup>65</sup> This reproducible reduction in both  $C_{ss}$  and  $R_{ct,ss}$  upon Co(II)/ $\text{Co}_3\text{O}_4$  modification was observed for

multiple batches of hematite and Co(II)/ $\text{Co}_3\text{O}_4$  depositions. In one rare case, the reduction in  $R_{ct,ss}$  was even greater, dipping as low as  $3 \times 10^3 \Omega \cdot \text{cm}$ , which is on par with the most efficient Co-Pi catalyst coatings on hematite to date—coatings that are less desirable due to thickness (300+ nm) and competitive light absorption.<sup>29</sup> The cathodic shift in the current onset potential, a reduced and shifted peak  $C_{ss}$ , and lower  $R_{ct,ss}$  for Co-modified photoelectrodes are all consistent with increased water oxidation kinetics. This conclusion is in contrast to that made by Cummings *et al.* for a different route to Co deposition, wherein the major role of  $\text{Co}^{2+}$  ions coated on hematite electrodes is believed to be reduction of surface-state recombination.<sup>39</sup> This may not be surprising given the distinct surface chemistry of the  $\text{Fe}_2\text{O}_3/\text{Co}(\text{II})/\text{Co}_3\text{O}_4$  electrochemical interface created by ALD. Evidence for less catalytic behavior in photoanodes with thicker overayers (Figure S2b) suggests the possibility of a synergistic effect of Co and Fe sites that is simultaneously electrochemically accessible. This behavior is in contrast to an increasingly more cathodic (dark) current onset when the same Co-based ALD process is applied to bare conductive glass (no hematite) (Figure S10).

## CONCLUSIONS

The coating of hematite nanolaminate photoanodes with a Co-based submonolayer by ALD results in a significant decrease in the applied potential required to drive photo-assisted water oxidation. The photocurrent onset potential shifted cathodically by 100–200 mV, and the photocurrent at 1.23 V increased for flat and inverse opal scaffold photoanodes. The photocurrent for the coated inverse opal scaffold reached over  $2 \text{ mA/cm}^2$  at 1.53 V vs RHE, representing one of the highest values achieved with a Co-based catalyst. Furthermore, the ALD-grown catalyst, which is shown to be Co(II) (hydr)oxide and  $\text{Co}_3\text{O}_4$ , exhibits important advantages over previous OER catalysts including no detectable optical absorption and promising stability. An investigation into the role of submonolayer Co(II)/ $\text{Co}_3\text{O}_4$  on hematite nanolaminate photoanodes was also performed with EIS. The combination of a reduction in the steady-state concentration of oxidized surface states, along with the reduction of charge transfer resistance from those surface states, reveals that the charge transfer kinetics from the surface of the photoanode to the electrolyte were accelerated with the addition of just 1 ALD cycle. This combination of catalytic activity, stability, optical transparency, and conformal deposition makes this a promising approach to improving the OER kinetics of photoanodes.

## EXPERIMENTAL SECTION

Conductive fluorine-doped tin oxide (FTO,  $15 \Omega \text{ cm}^{-2}$ , Hartford Glass, Co.) coated glass substrates were cleaned by a

gentle scrub with detergent, rinsed with DI water, sonicated in acetone for 10 min, followed by a 10 min sonication in isopropyl alcohol, and finally blown dry with a stream of  $\text{N}_2$ . Prior to

deposition, the FTO was loaded into the ALD chamber and ozone cleaned for 3 min. Silicon substrates for ellipsometric measurements were also cleaned using the procedure above less the detergent scrub. Inverse opal scaffolds were prepared on FTO-coated glass using a 2.6% stock solution of 350 nm polystyrene particles.<sup>71</sup> The resulting inverse opal scaffolds were 8 layers thick with a pore size of 300 nm. Prior to ALD, the scaffolds were treated with ozone for 3 min.

Tin-doped indium oxide (ITO) and  $\text{Fe}_2\text{O}_3$  depositions were carried out in a Cambridge Nanotech, Inc. Savannah 200 ALD reactor. The ALD reaction timing follows the sequence  $t_1 - t_2 - t_3 - t_4$ , where  $t_1$  and  $t_2$  are the exposure and purge times for precursor A (metal precursors) and  $t_3$  and  $t_4$  are the exposure and purge times for ozone. Note that the times are in seconds. Ferrocene ( $\text{Fe}(\text{Cp})_2$ , 98% Aldrich), cyclopentadienylindium(I) ( $\text{InCp}$ , 99.99%, Strem), tetrakis(dimethylamido)tin(IV) (TDMASn, 99.9%, Aldrich), and bis(cyclopentadienyl)cobalt(II) ( $\text{Co}(\text{Cp})_2$ , 98% Strem) were used without further purification. Ozone was generated by a DelOzone generator (5 wt % in 500 sccm ultrahigh-purity oxygen). The ALD conditions for ITO were as follows:  $\text{InCp}$  and TDMASn were heated to 70 and 55 °C, respectively, and the reaction chamber was 210 °C. Using a quasi-static exposure (no pumping) for the  $\text{InCp}$ , the sequence for the  $\text{In}_2\text{O}_3$  cycles was 30–35–65–25. Every 10th  $\text{InCp}$  cycle was replaced by a 15 s quasi-static exposure TDMASn cycle. The ALD ITO films were used without postdeposition processing.  $\text{Fe}_2\text{O}_3$  was deposited on the ITO-coated FTO substrates using the sequence 60–35–90–20. We note that the 60 s  $\text{Fe}(\text{Cp})_2$  exposure was split into two consecutive 30 s static exposures separated by a 5 s purge, and the 90 s ozone exposure was two consecutive 45 s pulses separated by a 1 s purge. Following deposition, the  $\text{Fe}_2\text{O}_3$  thin films were annealed at 500 °C for 30 min in flowing ultrahigh-purity  $\text{O}_2$  (250 sccm). The ramp rate was 10 °C/min. Films were coated with ALD  $\text{Co}(\text{II})/\text{Co}_3\text{O}_4$  using the pulsing sequence 30–35–90–25, where the 30 s  $\text{Co}(\text{Cp})_2$  exposure was two consecutive 15 s static exposures with a 5 s purge, and the 90 s ozone exposure was the same as that used for the ALD of  $\text{Fe}_2\text{O}_3$ . ITO,  $\text{Fe}_2\text{O}_3$ , and thick cobalt-based film thicknesses were estimated using a J.A. Woolam Co. M2000 variable-angle spectroscopic ellipsometer (VASE) from ellipsometric measurements on witness silicon chips.

Current–voltage (20 mV/s scan rate) and stability measurements were performed in 0.1 M KOH (Sigma, 99.99% semiconductor grade), pH 13.1, with a μAutolab Type III potentiostat. A three-electrode configuration was used, where the reference electrode was Ag/AgCl, and the counter electrode was a Pt wire. The  $\text{Fe}_2\text{O}_3$  films were masked with 60 μm transparent Surlyn (Solaronix) to define an active area of 0.38 cm<sup>2</sup>. A Newport 300 W arc lamp equipped with an AM 1.5 and UV filter was used as the light source, and the output power was calibrated with a Newport silicon photodiode (model 71580) to simulate AM 1.5 conditions (100 mW/cm<sup>2</sup>). A monochromator attached to the arc lamp was used for monochromatic light. Impedance measurements were measured at different applied bias using a perturbation amplitude of 10 mV. The frequency range was 10 kHz to 40 mHz. Data were fit using Zview software (Scribner Associates). The light source for impedance measurements was a 450 W Xe arc lamp (Horiba Jobin Yvon). Reflectance-corrected UV–vis data were collected on a Cary5000 UV–vis–NIR with an integrating sphere accessory.

X-ray photoelectron spectroscopy (XPS) was performed in a custom instrument with a Mg K $\alpha$  (1253.6 eV) X-ray source and a hemispherical electron energy analyzer in the fixed absolute resolution mode. A pass energy of 44 eV was used for both the survey spectra as well as for the detailed measurements of specific regions. The energy step for the survey spectra and the detailed measurements were 0.5 and 0.1 eV, respectively, with the exception of the  $\text{Co}_3\text{O}_4$  standard, where a 0.5 eV step was used for the detailed spectrum. XPS data were processed using CasaXPS (Copyright 2009 Casa Software, Ltd.). Gausian(70%)-Lorentzian(30%), defined as GL(30) in CasaXPS, line shapes were used for each component. All spectra were shifted to account for sample charging using adventitious carbon as a reference to 284.5 eV.  $\text{CoO}$ ,  $\text{Co}(\text{OH})_2$ , and  $\text{Co}_3\text{O}_4$  standards were obtained from Sigma Aldrich and used as received.

X-ray absorption near-edge spectroscopy (XANES) on the ALD sample, as well as full complement of cobalt standards, was performed at the 12-ID-C Beamline of the Advanced Photon Source at the Argonne National Laboratory at room temperature. The spectra were collected by a 4-element fluorescence detector (Vortex 4 element SDD) mounted parallel to the sample surface and perpendicular to the X-ray beam. A full complement of cobalt standards was collected at the 12-ID-C Beamline. The collected spectra were normalized, energy calibrated, and fitted using the Athena 0.8.056 package. A linear combination fitting was used to determine the contribution of standards which make up the analyzed sample.

*Conflict of Interest:* The authors declare no competing financial interest.

*Acknowledgment.* S.C.R., M.J.P., and A.B.F.M. acknowledge the ANSER Center, an Energy Frontier Research Center funded by the U.S. Department of Energy, Office of Science, Office of Basic Energy Sciences under Award Number DE-SC0001059 for support of this research. A portion of the research was performed at Argonne National Laboratory, a U.S. Department of Energy, Office of Science, Laboratory operated under Contract No. DE-AC02-06CH11357 by UChicago Argonne, LLC. T.W.H. acknowledges the National Science Foundation (CHE-1150378) for support of this research. The authors thank the Hupp lab at Northwestern University for the contribution of the inverse opal scaffolds. S.V. acknowledges the support by the U.S. Department of Energy, BES Materials Sciences, under Contract DE-AC-02-06CH11357, with UChicago Argonne, LLC, operator of Argonne National Laboratory. The use of the Advanced Photon Source, an Office of Science User Facility operated for the U.S. Department of Energy (DOE) Office of Science by Argonne National Laboratory, was supported by the U.S. DOE under Contract No. DE-AC02-06CH11357. E.C.T. acknowledges financial support by a MURI grant from the Air Force Office of Sponsored Research FA9550-08-0309.

*Supporting Information Available:* Additional UV–vis,  $J$ – $E$  curves, and EIS data. This material is available free of charge via the Internet at <http://pubs.acs.org>.

## REFERENCES AND NOTES

- Lewis, N. S.; Nocera, D. G. Powering the Planet: Chemical Challenges in Solar Energy Utilization. *Proc. Natl. Acad. Sci. U.S.A.* **2006**, *103*, 15729–15735.
- Ginley, D.; Green, M. A.; Collins, R. Solar Energy Conversion toward 1 Terawatt. *MRS Bull.* **2008**, *33*, 355–364.
- Bolton, J. R.; Strickler, S. J.; Connolly, J. S. Limiting and Realizable Efficiencies of Solar Photolysis of Water. *Nature* **1985**, *316*, 495–500.
- Walter, M. G.; Warren, E. L.; McKone, J. R.; Boettcher, S. W.; Mi, Q. X.; Santori, E. A.; Lewis, N. S. Solar Water Splitting Cells. *Chem. Rev.* **2010**, *110*, 6446–6473.
- Khaselev, O.; Turner, J. A. A Monolithic Photovoltaic-Photoelectrochemical Device for Hydrogen Production via Water Splitting. *Science* **1998**, *280*, 425–427.
- Bard, A. J.; Fox, M. A. Artificial Photosynthesis—Solar Splitting of Water to Hydrogen and Oxygen. *Acc. Chem. Res.* **1995**, *28*, 141–145.
- Fujishima, A.; Honda, K. Electrochemical Photolysis of Water at a Semiconductor Electrode. *Nature* **1972**, *238*, 37–38.
- Hamann, T. W. Splitting Water with Rust: Hematite Photoelectrochemistry. *Dalton Trans.* **2012**, *41*, 7830–7834.
- Lin, Y.; Yuan, G.; Sheehan, S.; Zhou, S.; Wang, D. Hematite-Based Solar Water Splitting: Challenges and Opportunities. *Energy Environ. Sci.* **2011**, *4*, 4862–4869.
- Sivula, K.; Le Formal, F.; Grätzel, M. Solar Water Splitting: Progress Using Hematite ( $\alpha\text{-Fe}_2\text{O}_3$ ) Photoelectrodes. *ChemSusChem* **2011**, *4*, 432–449.
- Kubacka, A.; Fernandez-Garcia, M.; Colon, G. Advanced Nanoarchitectures for Solar Photocatalytic Applications. *Chem. Rev.* **2012**, *112*, 1555–1614.

12. Turner, J. E.; Hendewerk, M.; Parmeter, J.; Neiman, D.; Somorjai, G. A. The Characterization of Doped Iron-Oxide Electrodes for the Photodissociation of Water: Stability, Optical, and Electronic-Properties. *J. Electrochem. Soc.* **1984**, *131*, 1777–1783.
13. Rajeshwar, K. Solar Energy Conversion and Environmental Remediation Using Inorganic Semiconductor–Liquid Interfaces: The Road Traveled and the Way Forward. *J. Phys. Chem. Lett.* **2011**, *2*, 1301–1309.
14. Katz, M. J.; Riha, S. C.; Jeong, N. C.; Martinson, A. B. F.; Farha, O. K.; Hupp, J. T. Toward Solar Fuels: Water Splitting with Sunlight and “Rust”? *Coord. Chem. Rev.* **2012**, *256*, 2521–2529.
15. Murphy, A. B.; Barnes, P. R. F.; Randeniya, L. K.; Plumb, I. C.; Grey, I. E.; Horne, M. D.; Glasscock, J. A. Efficiency of Solar Water Splitting Using Semiconductor Electrodes. *Int. J. Hydrogen Energy* **2006**, *31*, 1999–2017.
16. Bjorksten, U.; Moser, J.; Grätzel, M. Photoelectrochemical Studies on Nanocrystalline Hematite Films. *Chem. Mater.* **1994**, *6*, 858–863.
17. Chemelewski, W. D.; Hahn, N. T.; Mullins, C. B. Effect of Si Doping and Porosity on Hematite’s ( $\alpha$ -Fe<sub>2</sub>O<sub>3</sub>) Photoelectrochemical Water Oxidation Performance. *J. Phys. Chem. C* **2012**, *116*, 5256–5262.
18. Hahn, N. T.; Mullins, C. B. Photoelectrochemical Performance of Nanostructured Ti- and Sn-Doped  $\alpha$ -Fe<sub>2</sub>O<sub>3</sub> Photoanodes. *Chem. Mater.* **2010**, *22*, 6474–6482.
19. Hahn, N. T.; Ye, H.; Flaherty, D. W.; Bard, A. J.; Mullins, C. B. Reactive Ballistic Deposition of  $\alpha$ -Fe<sub>2</sub>O<sub>3</sub> Thin Films for Photoelectrochemical Water Oxidation. *ACS Nano* **2010**, *4*, 1977–1986.
20. Beermann, N.; Vayssieres, L.; Lindquist, S. E.; Hagfeldt, A. Photoelectrochemical Studies of Oriented Nanorod Thin Films of Hematite. *J. Electrochem. Soc.* **2000**, *147*, 2456–2461.
21. Kay, A.; Cesar, I.; Grätzel, M. New Benchmark for Water Photooxidation by Nanostructured  $\alpha$ -Fe<sub>2</sub>O<sub>3</sub> Films. *J. Am. Chem. Soc.* **2006**, *128*, 15714–15721.
22. Gemmer, J.; Hinrichsen, Y.; Abel, A.; Bachmann, J. Systematic Catalytic Current Enhancement for the Oxidation of Water at Nanostructured Iron(III) Oxide Electrodes. *J. Catal.* **2012**, *290*, 220–224.
23. Lin, Y. J.; Zhou, S.; Sheehan, S. W.; Wang, D. W. Nanonet-Based Hematite Heteronanostructures for Efficient Solar Water Splitting. *J. Am. Chem. Soc.* **2011**, *133*, 2398–2401.
24. Stefk, M.; Cornuz, M.; Mathews, N.; Hisatomi, T.; Mhaisalkar, S.; Grätzel, M. Transparent, Conducting Nb:SnO<sub>2</sub> for Host–Guest Photoelectrochemistry. *Nano Lett.* **2012**, *12*, 5431–5435.
25. Riha, S. C.; DeVries Vermeer, M. J.; Martinson, A. B. F.; Farha, O. K.; Pellin, M. J.; Hupp, J. T. Transparent Conducting Oxide Scaffolds for Hematite Water Oxidation Photoanodes. *ACS Appl. Mater. Interfaces* **2012**, *5*, 360–367.
26. Tilley, S. D.; Cornuz, M.; Sivula, K.; Grätzel, M. Light-Induced Water Splitting with Hematite: Improved Nanostructure and Iridium Oxide Catalysis. *Angew. Chem., Int. Ed.* **2010**, *49*, 6405–6408.
27. Le Formal, F.; Tetreault, N.; Cornuz, M.; Moehl, T.; Graetzel, M.; Sivula, K. Passivating Surface States on Water Splitting Hematite Photoanodes with Alumina Overlays. *Chem. Sci.* **2011**, *2*, 737–743.
28. Barroso, M.; Cowan, A. J.; Pendlebury, S. R.; Graetzel, M.; Klug, D. R.; Durrant, J. R. The Role of Cobalt Phosphate in Enhancing the Photocatalytic Activity of  $\alpha$ -Fe<sub>2</sub>O<sub>3</sub> toward Water Oxidation. *J. Am. Chem. Soc.* **2011**, *133*, 14868–14871.
29. Klahr, B.; Gimenez, S.; Fabregat-Santiago, F.; Bisquert, J.; Hamann, T. W. Photoelectrochemical and Impedance Spectroscopic Investigation of Water Oxidation with “Co-Pi”-Coated Hematite Electrodes. *J. Am. Chem. Soc.* **2012**, *134*, 16693–16700.
30. Xi, L.; Tran, P. D.; Chiam, S. Y.; Bassi, P. S.; Mak, W. F.; Mulmudi, H. K.; Batabyal, S. K.; Barber, J.; Loo, J. S. C.; Wong, L. H. Co<sub>3</sub>O<sub>4</sub>-Decorated Hematite Nanorods as an Effective Photoanode for Solar Water Oxidation. *J. Phys. Chem. C* **2012**, *116*, 13884–13889.
31. Sun, J. W.; Zhong, D. K.; Gamelin, D. R. Composite Photoanodes for Photoelectrochemical Solar Water Splitting. *Energy Environ. Sci.* **2010**, *3*, 1252–1261.
32. Zhong, D. K.; Sun, J. W.; Inumaru, H.; Gamelin, D. R. Solar Water Oxidation by Composite Catalyst/ $\alpha$ -Fe<sub>2</sub>O<sub>3</sub> Photoanodes. *J. Am. Chem. Soc.* **2009**, *131*, 6086–6087.
33. Zhong, D. K.; Cornuz, M.; Sivula, K.; Graetzel, M.; Gamelin, D. R. Photo-assisted Electrodeposition of Cobalt-Phosphate (Co-Pi) Catalyst on Hematite Photoanodes for Solar Water Oxidation. *Energy Environ. Sci.* **2011**, *4*, 1759–1764.
34. Zhong, D. K.; Gamelin, D. R. Photoelectrochemical Water Oxidation by Cobalt Catalyst (“Co-Pi”)/ $\alpha$ -Fe<sub>2</sub>O<sub>3</sub> Composite Photoanodes: Oxygen Evolution and Resolution of a Kinetic Bottleneck. *J. Am. Chem. Soc.* **2010**, *132*, 4202–4207.
35. McDonald, K. J.; Choi, K.-S. Photodeposition of Co-Based Oxygen Evolution Catalysts on  $\alpha$ -Fe<sub>2</sub>O<sub>3</sub> Photoanodes. *Chem. Mater.* **2011**, *23*, 1686–1693.
36. Li, J.; Meng, F.; Suri, S.; Ding, W.; Huang, F.; Wu, N. Photoelectrochemical Performance Enhanced by a Nickel Oxide–Hematite p-n Junction Photoanode. *Chem. Commun.* **2012**, *48*, 8213–8215.
37. Cesar, I.; Sivula, K.; Kay, A.; Zboril, R.; Graetzel, M. Influence of Feature Size, Film Thickness, and Silicon Doping on the Performance of Nanostructured Hematite Photoanodes for Solar Water Splitting. *J. Phys. Chem. C* **2009**, *113*, 772–782.
38. Steinmiller, E. M. P.; Choi, K.-S. Photochemical Deposition of Cobalt-Based Oxygen Evolving Catalyst on a Semiconductor Photoanode for Solar Oxygen Production. *Proc. Natl. Acad. Sci. U.S.A.* **2009**, *106*, 20633–20636.
39. Cummings, C. Y.; Marken, F.; Peter, L. M.; Tahir, A. A.; Wijayantha, K. G. U. Kinetics and Mechanism of Light-Driven Oxygen Evolution at Thin Film  $\alpha$ -Fe<sub>2</sub>O<sub>3</sub> Electrodes. *Chem. Commun.* **2012**, *48*, 2027–2029.
40. Peter, L. M.; Wijayantha, K. G. U.; Tahir, A. A. Kinetics of Light-Driven Oxygen Evolution at  $\alpha$ -Fe<sub>2</sub>O<sub>3</sub> Electrodes. *Faraday Discuss.* **2012**, *155*, 309–322.
41. Bakke, J. R.; Pickrahn, K. L.; Brennan, T. P.; Bent, S. F. Nanoengineering and Interfacial Engineering of Photovoltaics by Atomic Layer Deposition. *Nanoscale* **2011**, *3*, 3482–3508.
42. Elam, J. W. Coatings on High Aspect Ratio Structures. In *Atomic Layer Deposition of Nanostructured Materials*; Pinna, N., Knez, M., Eds.; Wiley-VCH Verlag & Co KGaA: Weinheim, Germany, 2012; pp 227–249.
43. Elam, J. W.; Libera, J. A.; Pellin, M. J.; Stair, P. C. Spatially Controlled Atomic Layer Deposition in Porous Materials. *Appl. Phys. Lett.* **2007**, *91*, 243105.
44. George, S. M. Atomic Layer Deposition: An Overview. *Chem. Rev.* **2010**, *110*, 111–131.
45. Kim, H.; Lee, H. B. R.; Maeng, W. J. Applications of Atomic Layer Deposition to Nanofabrication and Emerging Nano-devices. *Thin Solid Films* **2009**, *517*, 2563–2580.
46. Gamelin, D. R. Water Splitting: Catalyst or Spectator. *Nat. Chem.* **2012**, *4*, 965–967.
47. Zhao, Y.; Hernandez-Pagan, E. A.; Vargas-Barbosa, N. M.; Dysart, J. L.; Mallouk, T. E. A High Yield Synthesis of Ligand-Free Iridium Oxide Nanoparticles with High Electrocatalytic Activity. *J. Phys. Chem. Lett.* **2011**, *2*, 402–406.
48. Lin, Y. J.; Xu, Y.; Mayer, M. T.; Simpson, Z. I.; McMahon, G.; Zhou, S.; Wang, D. W. Growth of p-Type Hematite by Atomic Layer Deposition and Its Utilization for Improved Solar Water Splitting. *J. Am. Chem. Soc.* **2012**, *134*, 5508–5511.
49. Lutterman, D. A.; Surendranath, Y.; Nocera, D. G. A Self-Healing Oxygen-Evolving Catalyst. *J. Am. Chem. Soc.* **2009**, *131*, 3838–3839.
50. Barreca, D.; Massignan, C.; Daolio, S.; Fabrizio, M.; Piccirillo, C.; Armelao, L.; Tondello, E. Composition and Microstructure of Cobalt Oxide Thin Films Obtained from a Novel Cobalt(II) Precursor by Chemical Vapor Deposition. *Chem. Mater.* **2001**, *13*, 588–593.
51. Burriel, M.; Garcia, G.; Santiso, J.; Abrutis, A.; Saltyte, Z.; Figueras, A. Growth Kinetics, Composition, and Morphology

of  $\text{Co}_3\text{O}_4$  Thin Films Prepared by Pulsed Liquid-Injection MOCVD. *Chem. Vap. Deposition* **2005**, *11*, 106–111.

52. Jiménez, V. M.; Fernández, A.; Espínós, J. P.; González-Elipe, A. R. The State of the Oxygen at the Surface of Polycrystalline Cobalt Oxide. *J. Electron Spectrosc. Relat. Phenom.* **1995**, *71*, 61–71.

53. Shi, R.; Chen, G.; Ma, W.; Zhang, D.; Qiu, G.; Liu, X. Shape-Controlled Synthesis and Characterization of Cobalt Oxides Hollow Spheres and Octahedra. *Dalton Trans.* **2012**, *41*, 5981–5987.

54. Yang, H.; Ouyang, J.; Tang, A. Single Step Synthesis of High-Purity  $\text{CoO}$  Nanocrystals. *J. Phys. Chem. B* **2007**, *111*, 8006–8013.

55. Yang, J.; Liu, H.; Martens, W. N.; Frost, R. L. Synthesis and Characterization of Cobalt Hydroxide, Cobalt Oxyhydroxide, and Cobalt Oxide Nanodisks. *J. Phys. Chem. C* **2009**, *114*, 111–119.

56. Biesinger, M. C.; Payne, B. P.; Grosvenor, A. P.; Lau, L. W. M.; Gerson, A. R.; Smart, R. S. Resolving Surface Chemical States in XPS Analysis of First Row Transition Metals, Oxides and Hydroxides: Cr, Mn, Fe, Co and Ni. *Appl. Surf. Sci.* **2011**, *257*, 2717–2730.

57. Diskus, M.; Nilsen, O.; Fjellvag, H. Thin Films of Cobalt Oxide Deposited on High Aspect Ratio Supports by Atomic Layer Deposition. *Chem. Vap. Deposition* **2011**, *17*, 135–140.

58. Lee, S.; Di Vece, M.; Lee, B.; Seifert, S.; Winans, R. E.; Vajda, S. Oxidative Dehydrogenation of Cyclohexene on Size Selected Subnanometer Cobalt Clusters: Improved Catalytic Performance via Evolution of Cluster-Assembled Nanostructures. *Phys. Chem. Chem. Phys.* **2012**, *14*, 9336–9342.

59. Ferguson, G. A.; Yin, C.; Kwon, G.; Tyo, E. C.; Lee, S.; Greeley, J. P.; Zapol, P.; Lee, B.; Seifert, S.; Winans, R. E.; et al. Stable Subnanometer Cobalt Oxide Clusters on Ultrananocrystalline Diamond and Alumina Supports: Oxidation State and the Origin of Sintering Resistance. *J. Phys. Chem. C* **2012**, *116*, 24027–24034.

60. Lei, Y.; Mahmood, F.; Lee, S.; Greeley, J.; Lee, B.; Seifert, S.; Winans, R. E.; Elam, J. W.; Meyer, R. J.; Redfern, P. C.; et al. Increased Silver Activity for Direct Propylene Epoxidation via Subnanometer Size Effects. *Science* **2010**, *328*, 224–228.

61. Tyo, E. C.; Yin, C.; Di Vece, M.; Qian, Q.; Kwon, G.; Lee, S.; Lee, B.; DeBartolo, J. E.; Seifert, S.; Winans, R. E.; et al. Oxidative Dehydrogenation of Cyclohexane on Cobalt Oxide ( $\text{Co}_3\text{O}_4$ ) Nanoparticles: The Effect of Particle Size on Activity and Selectivity. *ACS Catal.* **2012**, *2*, 2409–2423.

62. Barroso, M.; Mesa, C. A.; Pendlebury, S. R.; Cowan, A. J.; Hisatomi, T.; Sivula, K.; Grätzel, M.; Klug, D. R.; Durrant, J. R. Dynamics of Photogenerated Holes in Surface Modified  $\alpha\text{-Fe}_2\text{O}_3$  Photoanodes for Solar Water Splitting. *Proc. Natl. Acad. Sci. U.S.A.* **2012**, *109*, 15640–15645.

63. Hisatomi, T.; Le Formal, F.; Cornuz, M.; Brillet, J.; Tetreault, N.; Sivula, K.; Graetzel, M. Cathodic Shift in Onset Potential of Solar Oxygen Evolution on Hematite by 13-Group Oxide Overlays. *Energy Environ. Sci.* **2011**, *4*, 2512–2515.

64. McDonald, K. J.; Choi, K. S. Synthesis and Photoelectrochemical Properties of  $\text{Fe}_2\text{O}_3/\text{ZnFe}_2\text{O}_4$  Composite Photoanodes for Use in Solar Water Oxidation. *Chem. Mater.* **2011**, *23*, 4863–4869.

65. Bertoluzzi, L.; Bisquert, J. Equivalent Circuit of Electrons and Holes in Thin Semiconductor Films for Photoelectrochemical Water Splitting Applications. *J. Phys. Chem. Lett.* **2012**, *3*, 2517–2522.

66. Klahr, B.; Giménez, S.; Fabregat-Santiago, F.; Hamann, T.; Bisquert, J. Water Oxidation at Hematite Photoelectrodes: The Role of Surface States. *J. Am. Chem. Soc.* **2012**, *134*, 4294–4302.

67. Tan, M. X.; Laibinis, P. E.; Nguyen, S. T.; Kesselman, J. M.; Stanton, C. E.; Lewis, N. S., Principles and Applications of Semiconductor Photoelectrochemistry. In *Progress in Inorganic Chemistry*; John Wiley & Sons, Inc.: New York, 2007; pp 21–144.

68. Lide, D. R. In *CRC Handbook of Chemistry and Physics*, 81st ed.; CRC Press/Taylor and Francis: Boca Raton, FL, 2001.

69. Glasscock, J. A.; Barnes, P. R. F.; Plumb, I. C.; Bendavid, A.; Martin, P. J. Structural, Optical and Electrical Properties of Undoped Polycrystalline Hematite Thin Films Produced Using Filtered Arc Deposition. *Thin Solid Films* **2008**, *516*, 1716–1724.

70. Klahr, B.; Giménez, S.; Fabregat-Santiago, F.; Bisquert, J.; Hamann, T. W. Electrochemical and Photoelectrochemical Investigation of Water Oxidation with Hematite Electrodes. *Energy Environ. Sci.* **2012**, *5*, 7626–7636.

71. Hatton, B.; Mishchenko, L.; Davis, S.; Sandhage, K. H.; Aizenberg, J. Assembly of Large-Area, Highly Ordered, Crack-Free Inverse Opal Films. *Proc. Natl. Acad. Sci. U.S.A.* **2010**, *107*, 10354–10359.